nature communications

Article

https://doi.org/10.1038/s41467-024-50679-1

Waste plastics upcycled for high-efficiency H_2O_2 production and lithium recovery via Ni-Co/carbon nanotubes composites

Received: 10 November 2023

Accepted: 18 July 2024

Published online: 01 August 2024

Check for updates

Baolong Qiu[1,5], Mengjie Liu[2,5], Xin Qu[3], Fengying Zhou[3], Hongwei Xie[1], Dihua Wang[3], Lawrence Yoon Suk Lee[2] ✉ & Huayi Yin[1,3,4] ✉

The disposal and management of waste lithium-ion batteries (LIBs) and low-density polyethylene (LDPE) plastics pose significant environmental challenges. Here we show a synergistic pyrolysis approach that employs spent lithium transition metal oxides and waste LDPE plastics in one sealed reactor to achieve the separation of Li and transition metal. Additionally, we demonstrate the preparation of nanoscale NiCo alloy@carbon nanotubes (CNTs) through co-pyrolysis of $LiNi_{0.6}Co_{0.2}Mn_{0.2}O_2$ and LDPE. The NiCo alloy@CNTs exhibits excellent catalytic activity (E_{onset} = ~0.85 V) and the selectivity (~90%) for H_2O_2 production through the electrochemical reduction of oxygen. This can be attributed to the NiCo nanoalloy core and the presence of CNTs with abundant oxygen-containing functional groups (e.g., −COOH and C−O−C), as confirmed by density function theory calculations. Overall, this work presents a straightforward and green approach for valorizing and upcycling various waste LIBs and LDPE plastics.

Lithium-ion batteries (LIBs) and plastics are playing an indispensable role in the advancement of a carbon-neutral society and improvement of our living standard[1–4]. However, the increasing costs and scarcity of raw materials for LIB production, along with the significant accumulation of waste batteries and plastics, present substantial challenges in our effort to build a sustainable and clean planet. Thus, there is a pressing need to shift towards a closed-loop critical element solution by recycling spent LIBs, rather than relying solely on natural metal reserves, and to develop green methods to address the issue of waste plastics[5–7]. While traditional metallurgical recycling processes have made notable progress in recent years, further advancements are still necessary to enhance their economic advantages and reduce environmental footprints[8]. One common trend in pyrometallurgical routes, which engage high thermal energy, is the reduction of operating temperature and the improvement of element extraction efficiency[9,10]. The use of novel reducing agents, such as H_2[11], CO[12], CH_4[13], and NH_3[14], has been extensively explored as these agents play a crucial role in determining the operating temperature and recovered products. Waste organics, including biomass[15], food wastes[16], and plastics[17,18], have been identified as promising reducing agents in some pyrolysis reduction reactions, enabling the co-recycling of spent LIBs and waste organics[19–21]. In addition to utilizing waste organics for producing gas to drive the reduction of lithium transition metal oxides (LTMOs), it is essential to understand the reduction process to maximize the recovery of carbon and critical metals.

Among various forms of organic wastes, low-density polyethylene (LDPE) plastic waste stands out as a heavily consumed materials and a prime candidate for recycling[22,23]. The abundant carbon sources present in plastic wastes can be utilized to promote the thermal reduction of spent LIBs[19], facilitate heat utilization[24,25], and contribute to the production of carbon materials[26]. Consequently, the synergistic pyrolysis of waste plastics and spent LIBs holds considerable potential as a

[1]Key Laboratory for Ecological Metallurgy of Multimetallic Mineral of Ministry of Education, School of Metallurgy, Northeastern University, Shenyang 110819, P. R. China. [2]Department of Applied Biology and Chemical Technology and Research Institute for Smart Energy, The Hong Kong Polytechnic University, Hung Hom, Kowloon, Hong Kong SAR, China. [3]School of Resource and Environmental Science, Wuhan University, Wuhan 430072, P. R. China. [4]Key Laboratory of Data Analytics and Optimization for Smart Industry, Ministry of Education, Northeastern University, Shenyang 110819, P. R. China. [5]These authors contributed equally: Baolong Qiu, Mengjie Liu. ✉e-mail: lawrence.ys.lee@polyu.edu.hk; yinhuayi@whu.edu.cn

sustainable alternative for the recycling of critical element, thereby reducing the need for detrimental landfilling and incineration of LIBs[27,28]. Additionally, the production of carbon materials from waste organics presents another avenue for enhancing the value of pyrolysis processes[29]. The pyrolysis gas derived from waste plastics offers a promising source for the production of carbon nanotubes (CNTs) through chemical vapor deposition (CVD), facilitated by the presence of metal catalysts such as Fe, Co, and Ni[30–33]. Notably, the main components present in LIB cathode materials have the potential to serve as catalysts for CNTs production[7,34]. Therefore, it is of great interest to prepare a composite consisting of TMs and CNTs using the pyrolysis approach. Through co-pyrolysis, the pyrolysis gas reduces LTMOs to TM and Li_2CO_3. Simultaneously, the resulting TMs can catalyze the decomposition of pyrolysis gas while also supplying carbon for the growth of CNTs on their surface. This co-pyrolysis has the potential to establish a paradigm-shifting concept of cross-domain upcycling, encompassing critical element recycling and the preparation of functional materials.

With the considerations outlined above, this work focuses on exploring efficient Li extraction and fabrication of metal/carbon materials through synergistic pyrolysis of spent LIBs and waste LDPE. A closed high-pressure reacting system is engaged to enable rapid reactions between decomposed pyrolysis gases and LTMO. This approach allows for the efficient extraction of Li (>98%), transformation of transition metals, and catalytic degradation of pyrolysis gas into solid carbon. Of particular significance are the CNT-encapsulated NiCo alloy products obtained from NCM622 ternary cathodes, which demonstrate excellent catalytic activity in electrochemical oxygen reduction to hydrogen peroxide. This finding underlines the potential value stream of upcycled functional materials. Furthermore, from both environmental and economic analysis, the co-pyrolysis process realizes the safe treatment of LDPE plastic wastes and the recovery and upcycling of spent LIBs.

Results

Co-pyrolysis of LTMO and LDPE

Figure 1a illustrates the distinctive layered structure of the reactor, which consists of a stainless-steel mesh in the middle, a chamber for waste plastics at the bottom, and another chamber for waste LIB cathode materials at the top. This configuration allows for the production and separation of Li_2CO_3 and metals such as Co, Mn, and Ni, as well as their alloys derived from various LTMOs (e.g., LCO, LMO, and NCM). Following pyrolysis, the LTMO, specifically NCM622, undergoes a transformation into NiCo alloy embedded on CNT (NiCo alloy@CNT),

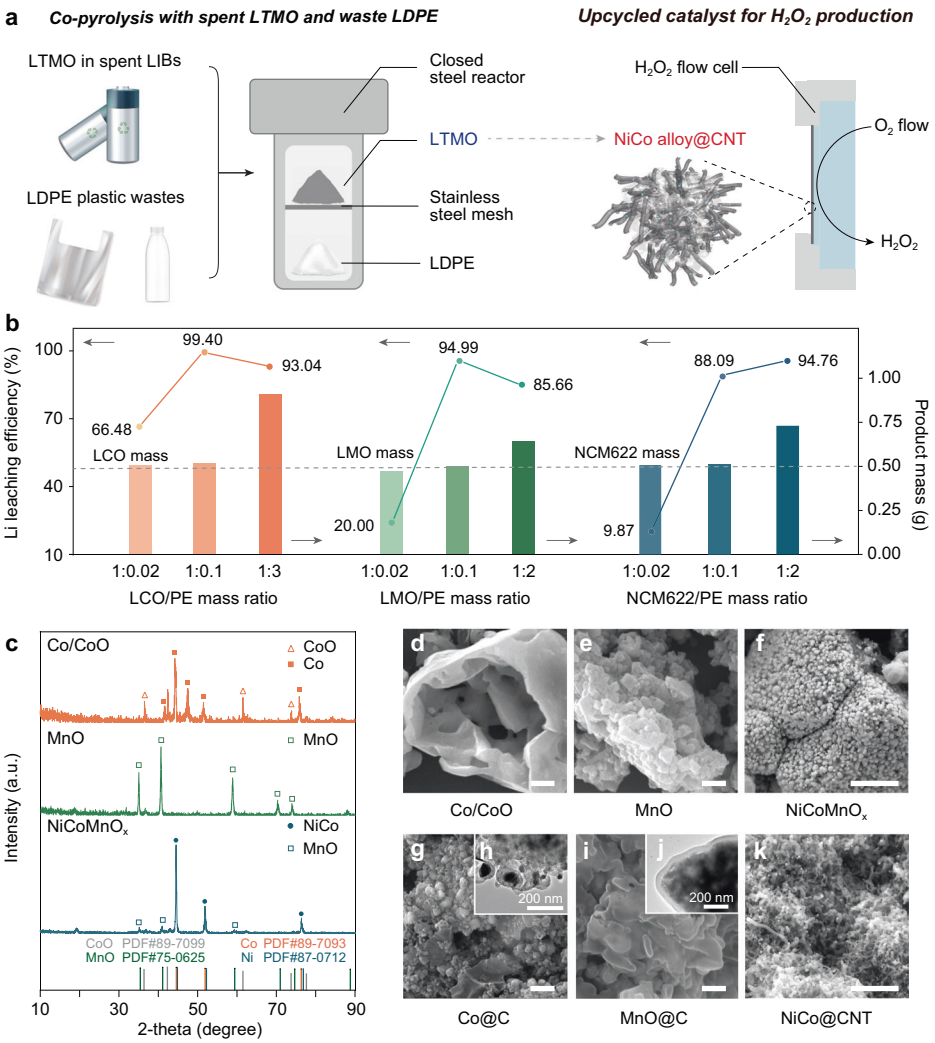

Fig. 1 | Waste LIB cathodes and LDPE plastic co-pyrolysis. a Conceptual design of the co-pyrolysis recycling process of spent LIB cathodes and LDPE plastic wastes, and their upcycling towards electrochemical H_2O_2 production; **b** Li leaching efficiency and mass of LTMO products under various LTMO/LDPE mass ratios. (500 °C, 5 h); **c** PXRD patterns of LTMO products using LTMO/LDPE mass ratio = 1:0.1. (500 °C, 5 h); SEM images of **d** LCO, **e** LMO, and **f** NCM622 using LTMO/LDPE mass ratio = 1:0.1 **g** LCO, **i** LMO, and (**k**) NCM622 using LTMO/LDPE mass ratio = 1:2 (500 °C, 5 h); scale bar is 1 μm. TEM images of **h** Co@C and **j** MnO@C.

which then serves as a catalyst for driving the electrochemical reduction of oxygen. Thermogravimetric-mass spectrometry (TG-MS) was employed under N_2 from 30 to 600 °C to perform an integrated analysis of LDPE mass loss and the molecular mass of the resulting pyrolysis gases. The major pyrolysis gases generated from LDPE include C_2H_4 (31.1%), H_2 (3.5%), C_2H_2 (1.2%), and C_2H_6 (0.5%) (Supporting Information: Figs. S1–2). Taking C_2H_4 as an example, the consumption of one mole of C_2H_4 as the reducing agent generates two moles of CO_2, which subsequently react with Li_2O to form Li_2CO_3, effectively solidifying the CO_2 and resulting in zero CO_2 emission. In contrast, conventional direct incineration emits 12 g of gaseous carbon per mol of LDPE (considering only the mass of carbon), which highlights the significant advantages of the co-pyrolysis system (Supporting Information: Fig. S3).

Through the fine-tuning of reaction temperature, time, and reactant mass ratio, the pyrolysis behaviors of the LTMO/benzene-free plastic (LLDPE, LDPE, and HDPE) systems are summarized in the Supporting Information: Figs. S4–10. Importantly, the amount of LDPE significantly influences the structural properties of the recovered TM/TMO and carbon materials, as well as the efficiency of Li leaching. Optimal conditions can be achieved by carefully balancing the amounts of reducing gases and LTMOs, thereby facilitating the complete reduction of LTMOs into metallic Ni/Co and MnO. In cases where LDPE pyrolysis gases are present in excess, they lead to additional carbon layer deposition on the previously reduced Ni/Co/MnO surface, resulting in the transformation of waste materials into carbon-coated metal products.

Figure 1b shows the Li leaching efficiency and the mass of LTMO recovery products, with varying LTMO/LDPE mass ratios of 1:0.02, 1:0.1, and 1:2 (or 1:3), representing insufficient, appropriate, and excess reducing agent conditions, respectively. With increasing LDPE content, LCO undergoes gradual reduction, resulting in the formation of CoO and subsequent metallic Co particles. Additionally, carbon originating from the excess organic gas undergoes transformation and gets deposited on the Co surface, leading to an increase in product weight from 0.51 to 0.91 g. This is supported by the appearance of an XRD peak corresponding to graphitic carbon at approximately 25°. However, excessive carbon deposition hinders further reactions and adversely affects the Li leaching rate. Based on atomic absorption spectrophotometry results, the highest Li leaching rate can reach up to 99.4% at an LTMO/LDPE mass ratio of 1:0.1. In the case of LMO, MnO is the final product due to the unfavorable thermodynamics of subsequent reduction to metallic Mn. Compared with Co, MnO exhibits weaker catalytic ability towards organic gases, resulting in lesser carbon deposition. In contrast to LCO and LMO, NCM622 can react with higher amount of LDPE without the hindrance of deposited carbon on Li extraction. The Li leaching efficiency continuously increases to 94.8% when twice the amount of LDPE is added. An intriguing phenomenon observed during NCM622/LDPE co-pyrolysis is the refinement/phase separation of TM/TMO particles and directional growth of CNTs following the deconstruction of cathode materials. The distinctive structural properties of the NCM622/LDPE products, differentiating them from the cases of LCO and LMO, may suggest a unique solid–gas reaction mechanism, which will be further discussed in detail.

Figure 1c compares the powder X-ray diffraction (PXRD) patterns of LCO, LMO and NCM622 products after pyrolysis and reduction at 500 °C, using an LTMO/LDPE mass ratio of 1:0.1. These reduction products are fully delithiated, resulting in the formation of TMO. The scanning electron microscopic (SEM) and transmission electron microscopic (TEM) images visualize the structural changes of cathode materials (Fig. 1d–f), which align with the PXRD and Li leaching efficiency results. In the case of LCO, significant structural damage occurs during the reaction with LDPE, causing the migration of Li, Co, and O atoms to the surface of the particles for further reactions. This results in the formation of a hollow CoO/Co structure. No obvious carbon deposition is observed under these conditions, which is confirmed by energy-dispersive X-ray (EDX) mapping. The Supporting information: Figs. S11–16 shows the SEM and TEM of LCO/LDPE and LMO/LDPE with different mass ratios. However, when a higher amount of LDPE (LCO/LDPE = 1:3) is introduced, the macroscopic hollow structure undergoes breakdown and refinement, yielding a small-sized Co yolk–C shell nanostructure (Co@C, Fig. 1g, h). Similarly, the upcycling of LMO initially generates carbon-free MnO (LMO/LDPE = 1:0.1), which then transforms into the MnO@C structure with a larger MnO core size (LMO/LDPE = 1:2) (Fig. 1i, j). In the case of NCM622, the initial reaction leads to the formation of metal active sites, and the increase in the amount of carbon deposition allows the growth of carbon nanotubes (Fig. 1k).

With the low feeding mass of LDPE, CoO/Co and MnO without carbon species are obtained from spent LCO and LMO, respectively. These products, along with recycled Li_2CO_3, can be directly utilized as raw materials for the regeneration of LIB cathodes through a roasting process (Supporting information: Fig. S17). In the case of NCM622, despite achieving high Li leaching efficiency under appropriate conditions, the mixture of NiCo alloy, MnO, and CNTs impedes the structure recovery through simple calcination. Consequently, they are not suitable as direct raw materials for cathode regeneration. However, the distinctive structure of CNTs and the presence of active metal species presents new opportunity for novel functional applications, such as electrochemical energy conversion. The production of metal/carbon composites with unique properties has significantly enhanced the competitiveness of our catalytic pyrolysis reactor systems for the upcycling of spent LIB materials.

The use of spent NCM622, serving as the pre-catalyst for CNT production, overcomes the size limitations associated with traditional CVD methods, which typically requires catalysts smaller than 100 nm for efficient CNT growth (Supporting information: Tables S1)[35–37]. The particle size of spent NCM622 is approximately 15–20 μm, which presents a theoretical challenge for CNT synthesis. In this study, we identified three stages of CNT growth during NCM622 catalytic pyrolysis (Fig. 2a). Firstly, the unique Li–O–TM layered structure of NCM622 serves as a natural template for the formation of Li salt. Under reducing conditions, Li ions in the Li–O units are extracted from the interlayer structure, leading to the formation of Li_2CO_3 on the boundaries of the delithiated TMO polycrystals. This process enables the retention of the nanoscale structure of intermediate products, preventing their agglomeration into larger particles. The Li salt can be easily removed by washing with water.

In the second stage, NiCo alloy is formed. SEM images of the products obtained by catalytic co-pyrolysis using various feeding ratios are provided in the Supporting information: Figs. S18, 19. When LDPE is present in insufficient quantities (NCM622/LDPE = 1:0.01), the resulting particles exhibit an average diameter of *ca.* 3–5 μm, similar to the pristine NCM622 precursors. These results are consistent with the unchanged XRD patterns observed. However, when NCM622/LDPE ratio is increased to 1:0.1, numerous nanoscale NiCo alloy and MnO particles, ranging from 80 to 100 nm in size, are formed on the surface. This indicates a phase separation and refinement process, taking place during the pyrolysis. To understand this phenomenon, the Mond method was employed to elucidate the refinement mechanism of NiO[38]. This mechanism involves the rapid formation of volatile nickel tetracarbonyl molecule ($Ni(CO)_4$) through the reaction between CO and reduced Ni. Under the same conditions, the formation of other metal carbonyl compounds is not observed. Subsequently, $Ni(CO)_4$ decomposes quickly into CO and small-sized Ni again, leading to the purification and refinement of metallic Ni particles from the initial NiO mixtures. It is believed that the refinement and separation of NiCo alloy from NCM622 follows a similar process, while MnO, due to its thermodynamically

https://doi.org/10.1038/s41467-024-50679-1

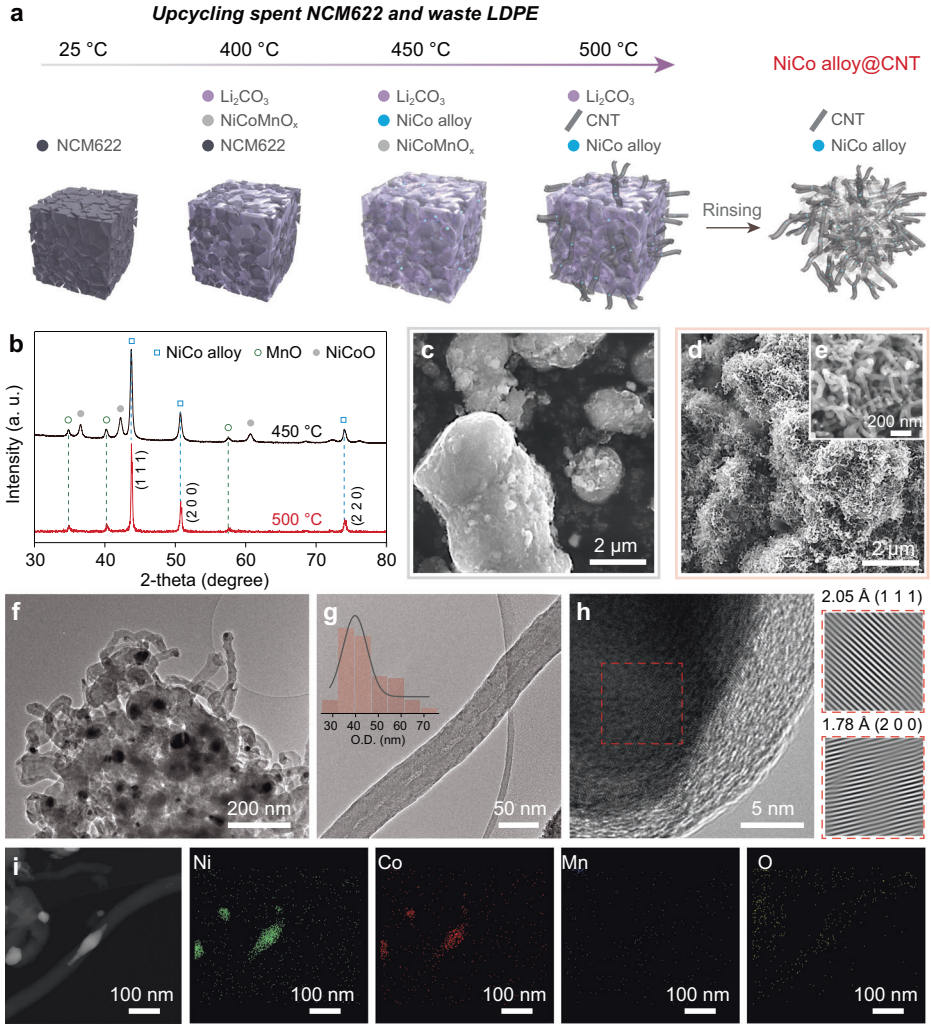

Fig. 2 | The upcycling mechanism of spent NCM622 to NiCo alloy@CNT. a A schematic illustration showing the upcycling mechanism of spent NCM622 and waste LDPE to NiCo alloy@CNT; **b** XRD patterns of $NiCoMnO_x$ and NiCo alloy@CNT produced at 450 and 500 °C, respectively. The corresponding SEM images of **c** $NiCoMnO_x$, **d** NiCo alloy@CNT, and **e** NiCo alloy@CNT; TEM images of **f** NiCo alloy@CNT and **g** CNT. Inset in **g** is the histogram of the outer diameter of nanotubes; **h** high-resolution TEM image of NiCo alloy@CNT. The lattice planes of the NiCo alloy (masked with red box) are shown on the right; **i** HAADF-STEM image and the corresponding EDX mapping images of NiCo alloy@CNT.

unfavorable reduction into Mn, is left behind and isolated from the NiCo phase.

The third process involves the controlled growth of CNTs, which resembles traditional CVD process. During this process, an excess of alkane gas, mainly C_2H_4, attaches to the nanoscale NiCo alloy particle templates, facilitating CNT nucleation and subsequent growth[30]. The temperature plays a crucial role in limiting the CNT growth (Fig. 2b). When spherical NiCo alloy particles with larger diameters are produced at 450 °C, they do not promote CNT formation (Fig. 2c). However, when the pyrolysis temperature is increased to 500 °C, CNTs become densely distributed across the field of view. Bright metal particles can be observed at the ends or within the tubes (Fig. 2d, e).

The TEM image of NiCo alloy@CNT displays metal nanoparticles encapsulated by CNTs (Fig. 2f). The intertwining nanotubes have an outer diameter ranging from 40 to 60 nm (Fig. 2g), primarily determined by the particle size of the inner NiCo alloy catalyst (*ca.* 30 nm). A representative high-resolution TEM image (Fig. 2h) reveals that the NiCo particles are anchored at the end of the CNT, indicating the catalytic role of the alloy in the epitaxial growth of CNTs. The corresponding inverse Fourier transformed (FT) images are indexed to the (111) and (200) lattice planes in hexagonal NiCo alloy, with the fringe spacings of 2.05 and 1.78 Å, respectively. High-angle annular dark-field (HAADF) scanning TEM and EDX elemental mapping images also confirm the composition of the catalyst encapsulated within the CNTs (Fig. 2i). The even distribution of Ni and Co, without any signal of Mn, suggests the successful separation of metal species in NCM622. Additionally, the presence of O signal along the CNT is observed, possibly resulting from residual O species during the reduction process of NCM622. The NiCo alloy@CNT exhibits a higher *D*-to-*G* peak intensity ratio (0.82) in the Raman spectrum compared with $NiCoMnO_x$@C (0.74), which indicates a higher level of disorder (i.e., defects) in its graphite structure (Supporting information: Fig. S20).

H_2O_2 Production by NiCo alloy@CNT

The CNTs in NiCo alloy@CNT contain abundant defects and oxygen functional groups, as confirmed by the Fourier-transform infrared spectroscopy (FTIR) and X-ray photoelectron spectroscopy (XPS). The FTIR spectrum in Fig. 3a displays peaks at 3438 cm^{-1} (O–H), 1780 cm^{-1} (C=O), and 1167 cm^{-1} (C–O), as well as aromatic ring characteristic peaks at 1450–1600 cm^{-1}. XPS full scan (Supporting information: Fig. S21) was engaged to investigate the chemical states of elements present on the surface of NiCo alloy@CNT. The C 1*s* spectrum (Fig. 3b) can be deconvoluted into five bands: carbon in graphite (284.5 eV), defects arising from missing carbon atoms (285.4 eV), C–O species

https://doi.org/10.1038/s41467-024-50679-1

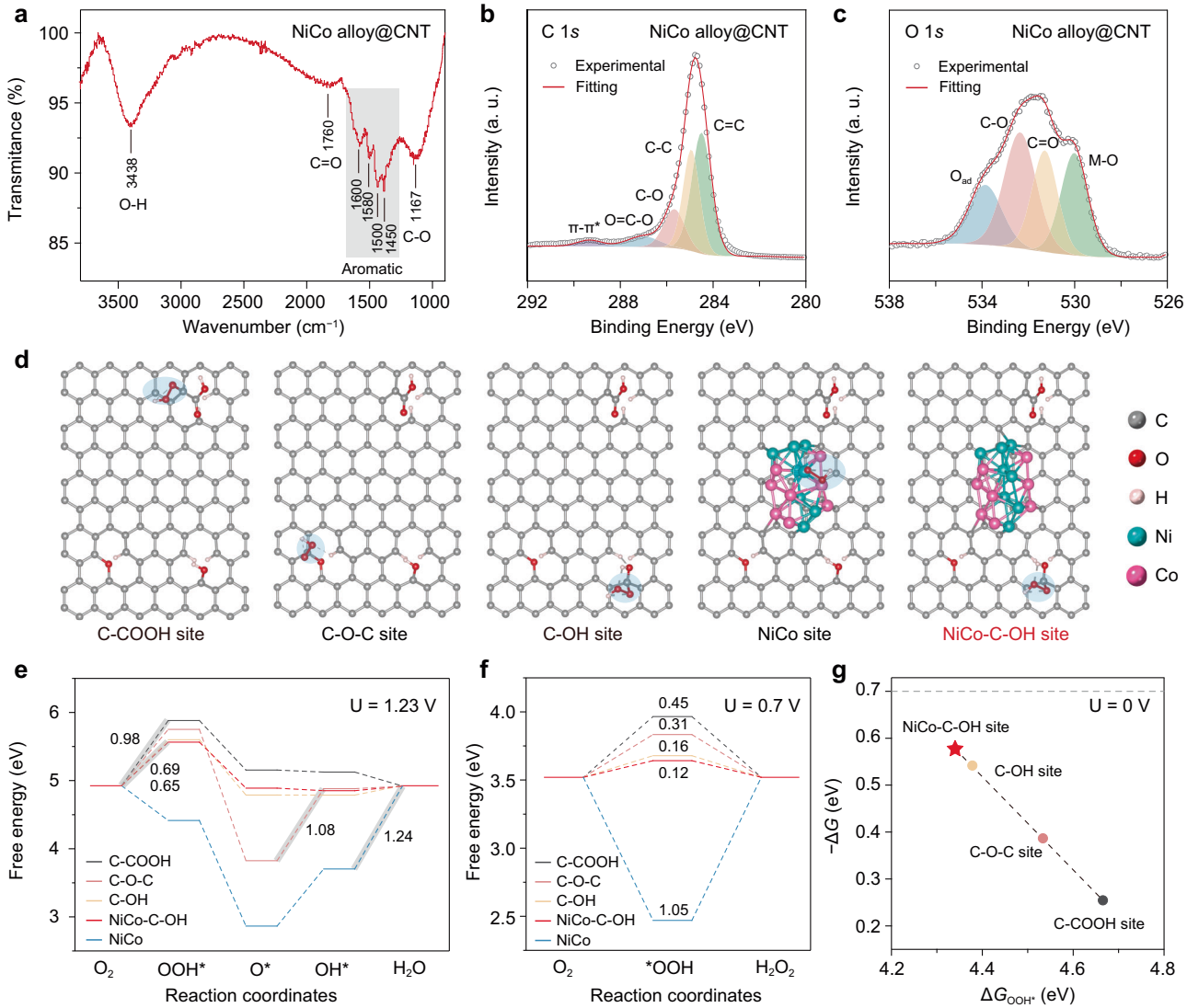

Fig. 3 | Model construction and DFT calculation of various oxygen functional groups in NiCo alloy@CNT. a FTIR, **b** C 1*s*, and **c** O 1*s* spectra of NiCo alloy@CNT. **d** Configurations of various oxygen functional groups examined in this study. Carbon atoms denoted by a blue circle are the active sites under investigation. The corresponding free energy diagrams for ORR at **e** $U = 1.23$ V, pH = 0 and **f** $U = 0.7$ V, pH = 0. **g** Calculated catalytic activity volcano plot (weak adsorption side) for the production of H_2O_2 via ORR.

(286.1 eV), carbon bonded with two oxygens (*i.e.*, –COOH, 288.7 eV), and the characteristic vibration line of carbon in aromatic compounds (π–π* transition, 290.5 eV). Peaks at around 530 eV indicate the presence of O 1*s* (Fig. 3c), resulting in a C-to-O ratio of 8.7:1 in CNTs, which significantly differs from commercial CNTs that have negligible oxygen content. Deconvolution of the O 1*s* spectrum reveals four peaks: oxygen double-bonded to carbon (C=O) at 531.6 eV, oxygen single-bonded to carbon (C–O) at 533.2 eV, lattice oxygen in MnO (523.0 eV), and the adsorbed oxygen (533.9 eV)[39–41].

The presence of abundant oxygen functional groups in carbon materials can significantly influence the oxygen reduction reaction (ORR) activity by modifying their electronic structure[39,40]. Understanding the active sites involved in the catalytic ORR process is crucial for gaining mechanistic insights and facilitating the rational design of catalysts. In this study, density functional theory (DFT) calculations were employed to investigate the ORR catalytic behaviors of various sites. To facilitate the analysis, two-dimensional graphene sheets were used as a model system, incorporating oxygen functional groups such as carboxyl (–COOH), carbonyl (C–O–C), hydroxyl (–OH), and/or NiCo alloys. Five different configurations were selected for comparison, which are depicted in Fig. 3d and Supporting information: Fig. S22. The ORR catalytic performance is strongly influenced by the binding affinity of catalyst toward ORR intermediates (OOH*, O, and OH*). As a result, the binding energy between the reaction intermediate and the active site of the catalyst (represented by the blue circle in Fig. 3d, binding with OOH*) determines the catalytic activity of different structures.

The ORR can proceed via two pathways: 4-electron ($4e^-$) or 2-electron ($2e^-$) pathway. In the energy diagram shown in Fig. 3e, which involves four coupled proton-electron transfers, the rate-limiting steps for C–COOH, C–OH, and NiCo–C–OH are the adsorption of OOH*, with energy barriers of 0.98, 0.69, and 0.65 eV, respectively. The rate-determining step for C–O–C involves the binding of OH*, requiring an energy of 1.08 eV. In NiCo alloy, the desorption of OH* requires an uphill of 1.24 eV. In the ORR pathway involving two electrons (Fig. 3f), the rate-determining steps for C–COOH, C–O–C, and C–OH occur at OOH*, with the corresponding energy barriers of 0.45, 0.31, and 0.16 eV, respectively. When NiCo alloy is present nearby, the binding energy on the surrounding O-containing functional groups decreases. Notably, the required energy for NiCo–C–OH with OOH* is reduced to 0.12 eV. Figure 3g illustrates the weak adsorption leg of the ORR

https://doi.org/10.1038/s41467-024-50679-1

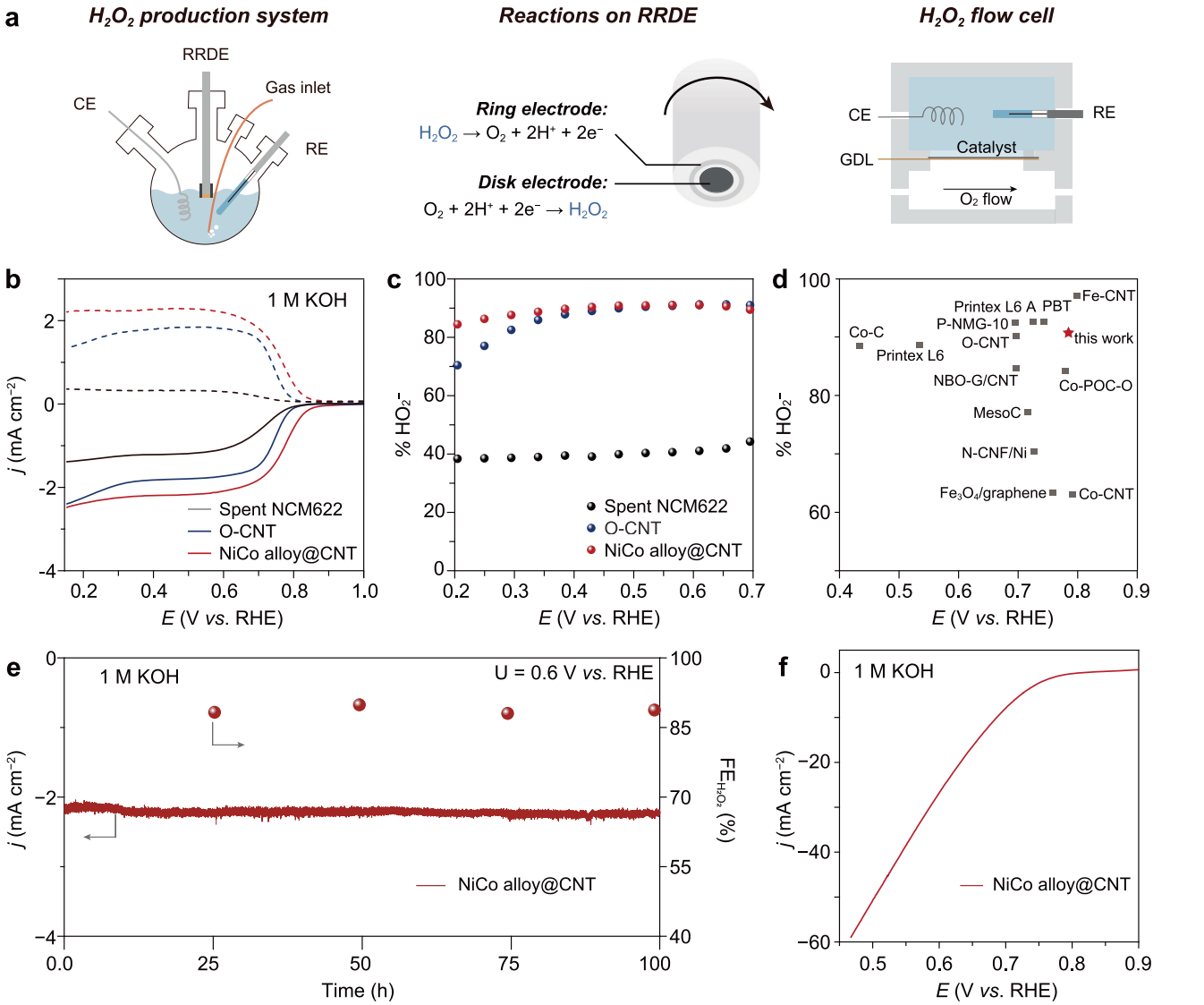

Fig. 4 | ORR performances of NiCo alloy@CNT. a Schematics of a three-electrode electrochemical cell and a gas diffusion flow cell. **b** Polarization curves of NiCo alloy@CNT, O-CNT, and spent NCM622 at 1600 rpm in O_2-saturated 1 M KOH and **c** calculated selectivity at various potentials in O_2-saturated 1 M KOH. **d** Comparison of reactivity and selectivity of H_2O_2 electrosynthesis. **e** Chronoamperometric response of NiCo alloy@CNT in an H-type cell. **f** Flow cell. The voltages in this figure are not iR corrected.

volcano plot, where the limiting potential is plotted as a function of OOH* adsorption energy (ΔG_{OOH^*}). The introduction of NiCo alloy reduces the adsorption energy barrier of C−OH to OOH*, potentially due to charge modulation and the corresponding shifts of Fermi level and *d*-band. We offer carboxylic acid treated CNTs and hydroxylated CNTs for reference (Supporting information: Fig. S23).

With the guidance of theoretical simulations, we evaluated ORR performances of NiCo alloy@CNT, commercial carboxylated CNT (denoted as O-CNT) and spent NCM622 using a three-phase flow cell and a rotating ring-disk electrode (RRDE) in an O_2-saturated high-purity 1 M KOH (Fig. 4a). The preferred ORR pathway in this study is the $2e^-$-pathway for efficient production of H_2O_2. The RRDE voltammograms in Fig. 4b present the oxygen reduction currents measured on the disk electrode (solid lines) and the H_2O_2 oxidation currents measured on the Pt ring electrode (dashed lines). The polarization curves of NiCo alloy@CNT exhibit the lowest onset potential (E_{onset}, 0.85 V vs. reversible hydrogen electrode, RHE) compared with the spent NCM622 (0.77 V) and O-CNT (0.78 V). Importantly, its limiting current rapidly increases to 2.49 mA cm^{-1}, which is much higher than those of O-CNTs (1.88 mA cm^{-1}) and NCM622 (1.16 mA cm^{-1}). Furthermore, NiCo alloy@CNT demonstrates larger ring currents, suggesting its highest selectivity for H_2O_2 production (~90%) compared with NCM622 (~40%) within the potential range of 0.2 and 0.7 V (Fig. 4c). The $2e^-$-reduction selectivity of O-CNT decreases to 65% at lower potentials, while NiCo alloy@CNT exhibits good stability across a wide potential window. The calculation of the electron transfer number (Supporting information: Fig. S24) confirms that NiCo alloy@CNT follows a standard $2e^-$-pathway. To investigate the contribution of surface metal species (NiCo) to the ORR catalytic activity, NiCo alloy@CNT was treated with 2 M HCl for 2 h to remove a majority of the surface metal (Supporting information: Fig. S25). Compared with the NiCo alloy@CNT, the E_{onset} and half-wave potential ($E_{1/2}$) shift negatively by 40 mV, indicating the positive contributions of the metal species (NiCo) on the ORR catalytic activity. The $2e^-$ selectivity of NiCo alloy@CNTs obtained by controlling the temperature at 600 °C and 800 °C is lower than that of NiCo alloy@CNTs obtained at 500 °C. This is mainly due to changes in the content of oxygen-containing functional groups (Supporting information: Fig. S26). NiCo alloy@CNT demonstrates a superior H_2O_2 production than Co@C (~60%) and MnO@C (~40%, Supporting information: Fig. S27).

https://doi.org/10.1038/s41467-024-50679-1

a **Table 1 Co-pyrolysis processes of various waste plastic and spent LIBs**

	LCO				*LMO*				*NCM622*			
	Temp (°C)	Mass ratio	Re-Li (%)	Re-M/MO	Temp (°C)	Mass ratio	Re-Li (%)	Re-M/MO	Temp (°C)	Mass ratio	Re-Li (%)	Re-M/MO
LDPE	500	1:0.1	99.2	Co/CoO	550	1:0.1	100	MnO	500	1:0.5	98.1	NiCo@CNT,MnO
PC	500	1:3	98.3	Co@C	550	1:0.1	99.5	MnO	500	1:3	97.5	NiCo,$MnCO_3$@C
PET	500	1:3	92.9	Co/CoO@C	500	1:0.1	94.9	MnO	500	1:3	94.9	NiCoMnO_x@C
PBT	500	1:3	94.3	Co@C	500	1:0.1	97.5	MnO	500	1:3	95.5	NiCoMnO_x@C
PS	500	1:3	81.5	CoO/Co	500	1:0.1	63.6	Li_2MnO_3	500	1:3	73.6	NiCo,MnO@C
PVC	450	1:1	92.5	$CoCl_2$								

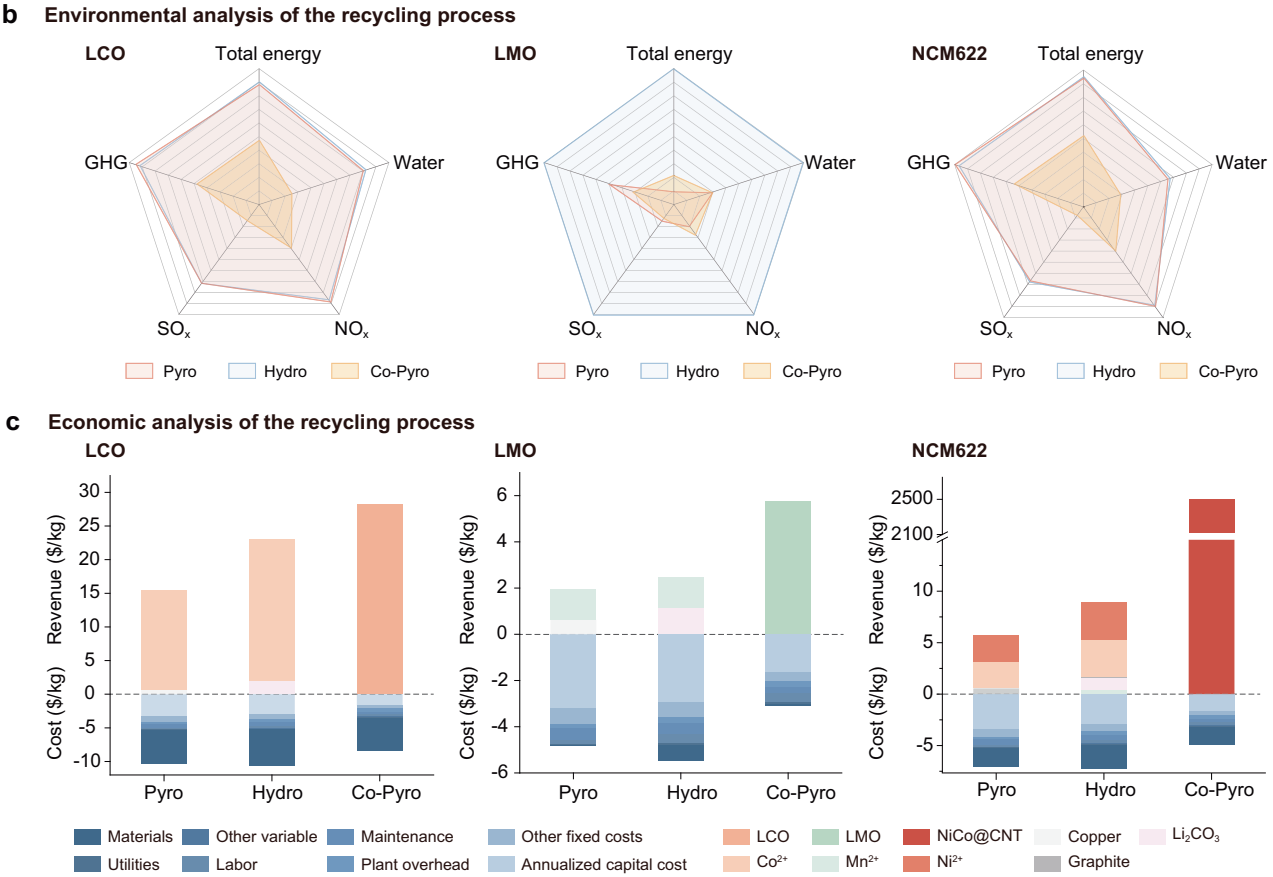

Fig. 5 | Environmental and economic analysis of the co-pyrolysis process of waste LIB cathodes and plastics. a Co-pyrolysis recovery conditions, Li extraction rate, and product phase of six plastic wastes (LDPE, PC, PET, PBT, PS, and PVC) and three spent LIB cathodes (LCO, LMO, and NCM622). Economic and environmental analysis of pyrometallurgical (Pyro), hydrometallurgical (Hydro), and co-pyrolysis (Co-Pyro) recycling methods: **b** Environmental analysis of the LCO, LMO, and NCM622 recycling processes and **c** the corresponding economic analysis.

The excellent $2e^-$ selectivity and rapid reaction rate of NiCo alloy@CNT make it a promising catalyst for practical H_2O_2 synthesis applications. To enhance the ORR current and overcome the limited oxygen mass transfer, the catalysts were loaded onto a hydrophobic carbon fiber paper and assembled in a large-scale gas diffusion flow cell, creating abundant three-phase contact points. Figure 4d compares the performances of NiCo alloy@CNT with recently reported state-of-the-art catalysts, highlighting the advantages of NiCo alloy@CNT in electrochemical H_2O_2 production (Supporting information: Table S2). The H_2O_2 production of NiCo alloy@CNT was further evaluated in a custom-made electrochemical H-type cell in 1 M KOH and the H_2O_2 concentration was determined through titration with Ce^{4+} ions (Fig. 4e). In a 100-hour electrolysis at 0.6 V, NiCo alloy@CNT demonstrates a stable operation with negligible current decline, achieving a high Faradaic efficiency of 88% and a H_2O_2 yield of 343.16 mmol g^{-1} h^{-1} (Supporting information: Fig. S28). In the polarization curve shown in Fig. 4f, the electrode attains the current densities of 20 and 40 mA cm^{-2} at 0.63 and 0.54 V, respectively, while maintaining a high H_2O_2 production selectivity of over 90%.

Economic and environmental analysis

The economic and environmental impacts of the plastic waste/spent LIBs cathode co-pyrolysis process were analyzed using the Everbatt model 2023. The analysis encompasses the process parameters, Li recovery rates, and product phases reported in previous studies[42]. The results indicate that LDPE, PC, PET, PBT, and PVC can achieve Li extraction efficiencies of over 90% from spent LIBs materials (LCO, LMO, and NCM622). This demonstrates the feasibility of implementing the co-pyrolysis process on an industrial scale (Fig. 5a).

Assuming an annual processing capacity of 2000 GWh of spent LIBs at a plant in China, three different recycling methods were modeled: pyrometallurgical (Pyro), hydrometallurgical (Hydro), and co-pyrolysis (Co-Pyro). Environmental analysis comparing three methods reveals the significant advantages of the co-pyrolysis process in terms of total energy consumption, water consumption, and greenhouse gas emissions (GHG, Fig. 5b). Furthermore, the co-pyrolysis process demonstrates the highest profitability among the three recycling methods. In particular, NiCo alloy@CNT upcycled from spent NCM622 generates profits as high as $2496 per kg (Fig. 5c). This substantial profit potential enhances the economic competitiveness of upcycling spent LIBs through co-pyrolysis (Supporting information: Tables S3–8).

Discussion

The co-pyrolysis of spent LIBs and LDPE wastes was performed in a closed operating system, maintaining a continuous gas/solid reaction interface. This process achieves complete conversion at relatively low pyrolysis temperature (500–550 °C). To prevent contamination from impurities in the waste plastics, physical separation of the waste plastics and spent LIBs was implemented at different positions within the reactor. The recovery of Li was accomplished in the form of Li_2CO_3 with an efficiency exceeding 98.0%, and no mineral acids were used in the process. CoO/Co and MnO, obtained from LCO and LMO, respectively, were directly recycled as raw materials for regeneration of LIB cathodes. Notably, the reducing pyrolysis gases from LDPE were employed to facilitate phase deconstruction of pristine cathodes, particle refinement, and separation of NiCo alloy and MnO products in NCM622. Additionally, this process promoted the directional growth of CNTs containing rich oxygen functional groups and defects. The resulting CNTs-encapsulated NiCo alloy exhibited a high selectivity (~90%) and onset potential (~0.85 V) for H_2O_2 production through electrochemical oxygen reduction. In summary, a smart upcycling solution is proposed, which utilizes LDPE wastes for the treatment of spent LIBs. This approach addresses the environmental challenges associated with waste LDPE disposal, recovery of valuable metal sources, and production of functional catalysts from spent LIBs, demonstrating a general and environmentally benign method for treating waste plastic and spent LIBs in waste electronics.

Methods

Chemicals and materials

Three commercial (AR grade) LTMO cathode materials, layered oxide $LiCoO_2$ (LCO), spinel oxide $LiMn_2O_4$ (LMO), and layered oxide $LiNi_{0.6}Co_{0.2}Mn_{0.2}O_2$ (NCM622) were purchased from Sinopharm Group Co. Ltd. Low-density polyethylene (LDPE, >99.9%) was obtained from Fengtai Polymer Materials Co. Ltd. Plastic bag wastes were collected from the Northeastern University. All materials were used as received without further purification.

Recovery of spent LIB cathodes

The co-pyrolysis recovery was carried out using a 50 mL steel reactor heated in a muffle furnace. LTMO (LCO, LMO, and NCM622) was selected as the representative electrode material for pyrolysis reduction. Initially, LTMO (0.5 g) was placed on a stainless steel, while varying amounts of LDPE ranging from 0.05 to 2 g were separately positioned at the bottom of the reactor. The operating temperature was maintained within a range of 400–550 °C (±0.1 °C) for different durations, ranging from 10 to 300 min, with a heating rate of 5 °C min^{-1}. Following the pyrolysis, the products on the stainless steel were transferred into a 100 mL beaker containing 50 mL of ionized water and stirred at 25 °C for 1 h. The solution was then poured into a funnel lined with a hydrophilic polyvinylidene hard pore membrane filter (d = 90 mm, pore size = 0.45 μm), and the resulting leachate was collected in a 100 mL volume flask to separate the filtrate and solid product. The filtrate was analyzed to determine the leaching efficiency of Li and Co, while the solid product was vacuum-dried at 60 °C for 24 h. The leaching efficiency (R_i) was calculated using Eq. (1):

$$R_i\,(\%) = \frac{\text{moles of recovered element i}}{\text{moles of an element in mixed powder}} \times 100 \quad (1)$$

To determine the contents of Li, Ni, Co, and Mn in the raw materials, the cathode materials were completely dissolved using aqua regia. Standard solutions of each element were prepared to calibrate the concentration curve. All solutions used in the experiment were prepared using deionized water, and all chemical reagents used were analytical grade.

Sample preparation and electrochemical characterization

The NCM622/LDPE mass ratio = 1:2, (500 °C, 5 h) water-washed sample was used as the catalyst sample. The electrodes were prepared by dispersing the catalysts in ethanol to obtain a concentration of approximately 10 mg mL^{-1} with 5 wt.% Nafion. After sonication for 60 min, 10 μL of the catalyst ink was drop-dried onto a glassy carbon disk (area = 0.2475 cm^2). The electrochemical tests were conducted using a PINE Wavedriver potentiostat in a three-electrode cell at room temperature (25 °C). A rotating ring disk electrode (RRDE) was used as the working electrode, while Pt foil and Hg/HgO in 1 M KOH were used as the counter and reference electrodes, respectively. A pH ~14 (1 M high purity KOH) electrolyte was chosen. The ORR activity and selectivity were investigated by polarization curves at a scan rate of 10 mV s^{-1} in an O_2-saturated electrolyte. Polarization curves in N_2-saturated electrolytes were also recorded to subtract the background signal. Flow-cell polarization curves were determined on hydrophobic carbon fiber paper (Toray, TGP-H-060) loaded with NiCo alloy@CNT at a loading density of approximately 0.5 mg cm^{-2}. The H_2O_2 yield was determined using an H-type electrolytic cell, where both the cathodic and anode compartments (50 mL) were filled with the same electrolyte (1 M KOH) at the room temperature (25 °C).

The H_2O_2 selectivity of NCM@CNT was calculated using the disk and ring currents collected on the RRDE according to Eq. (2).

$$H_2O_2\ \text{selectivity}{:}H_2O_2(\%) = 200 \times \frac{I_R/N}{I_D + I_R/N} \quad (2)$$

where I_R is the ring current, I_D is the disk current, and N is the collection efficiency (0.37 after calibration). The ring electrode was subjected to an applied potential of 1.4 V (*vs.* RHE) and rotated at a rate of 1600 rpm throughout the test.

H_2O_2 concentration measurement

A yellow transparent solution of $Ce(SO_4)_2$ (1 mM) was prepared by dissolving 33.2 mg of $Ce(SO_4)_2$ in 100 mL of 0.5 M H_2SO_4 solution. To construct the calibration curve, a series of known concentrations of H_2O_2 were added to the $Ce(SO_4)_2$ solution, and the resulting mixtures were quantified using ultraviolet-visible (UV-vis) spectroscopy. After performing a chronoamperometry test under 0.6 V vs. RHE for 25 hours, 0.1 mL of the electrolyte was added to 8.9 mL of a pre-calibrated 0.5 mM $Ce(SO_4)_2$ solution. The H_2O_2 concentration was determined using a conventional titration method using $Ce(SO_4)_2$, where the yellow solution of Ce^{4+} is reduced to colorless Ce^{3+} by the reaction with H_2O_2 (Eq. 3).

$$2Ce^{4+} + H_2O_2 \rightarrow 2Ce^{3+} + 2H^+ + O_2 \quad (3)$$

The H_2O_2 amount in 0.1 mL of sample electrolyte was quantified using a linear correlation established between the absorbance at 316 nm and

the Ce^{4+} concentration ranging from 0.01 to 0.5 mM. Therefore, the H_2O_2 concentration (C) can be determined by Eq. (4)

$$C(H_2O_2) = 1/2M\,Ce^{4+}/V_{electrolyte} \quad (4)$$

The resulting H_2O_2 amount in all electrolytes was then divided by the catalyst mass and total charge time to obtain the H_2O_2 yield according to Eq. (5)

$$H_2O_2\ \text{yield} = \frac{C(H_2O_2) \times V_{all\ telectrolyte}}{m_{loading\ catalysts} \times h} \quad (5)$$

The Faradaic efficiency (FE_{H2O2}) can be calculated by the concentration of hydrogen peroxide times the volume of the H-Cell cathode tank times the number of electrons transferred divided by the total charge Q, according to Eq. (6).

$$FE_{H_2O_2} = \frac{2e^- \times C(H_2O_2) \times V_{all\ electrolyte} \times 96500}{Q} \quad (6)$$

Characterizations

The crystal phases and components of all pyrolysis products were analyzed using a Rigaku-T III X-ray diffractometer (XRD, Shimadzu X-ray 6000) equipped with Cu Kα radiation of 1.5406 Å at a scan rate of 10° min^{-1} over a 2θ range from 10 to 90°. The concentrations of Li^+, Co^{2+}, Mn^{2+}, and Ni^{2+} in the solutions were determined using an atomic absorption spectrophotometer (AAS, TAS-990). Thermogravimetry-differential scanning calorimeter (TG-DSC) was used to analyze the thermal process (NETZSCH STA 449F5). Thermogravimetry-mass spectrometry (TG-MS) was performed using a thermal analyzer (Thermo plus EV2/thermo mass photo) from 30 to 600 °C at a heating rate of 10 °C min^{-1}, while N_2 gas was passed through the cavity at a flow rate of 300 mL min^{-1}. Pyrolysis gases were analyzed using gas chromatography (GC, 9790H, Zhejiang Fuli, Analytical Inc.). A scanning electron microscope (SEM, FEI Quanta FEG 250) and a transmission electron microscope (TEM, JEOL Model JEM-2100F, 200 kV) were used to characterize the morphology and composition of materials. Raman spectra were recorded on a confocal micro-Raman spectroscopy system (Renishaw, inVia) with a 532 nm streamline laser excitation. XPS was conducted on an X-ray photoelectron spectrometer (Thermo Scientific K-Alpha) and the data were analyzed using CasaXPS software.

Thermodynamic calculations

The standard Gibbs free energy, $\triangle_r G_T^\theta$, can be expressed as:

$$\triangle_r G = \triangle r G_T^\theta + RT\ln\left(K_{PB/P^\theta}\right) \quad (7)$$

where $\triangle_r G$ represents the Gibbs free energy of a certain reaction; R is the universal gas constant, 8.314 J mol^{-1} K^{-1}; T is the absolute temperature; K_{P_B/P^θ} represents gas pressure equilibrium constant. When a chemical reaction reaches its equilibrium state, $\Delta_r G = 0$ or $\triangle_r G_T^\theta = -RT\ln K$, while $\Delta_r G < 0$ indicates that the chemical reaction is spontaneous.

Thermal reduction involving C_2H_4:

$$12LiCoO_2 + C_2H_4(g) \rightarrow 12CoO + 6Li_2O + 2CO_2(g) + 2H_2O(g) \quad (8)$$

$$12LiNi_{0.6}Co_{0.2}Mn_{0.2}O_2 + C_2H_4(g) \rightarrow 12/5CoO + 36/5NiO + 12/5MnO + 6Li_2O + 2CO_2(g) + 2H_2O(g) \quad (9)$$

$$36/5LiMn_2O_4 + C_2H_4(g) \rightarrow 18/5Li_2O + 24/5Mn_3O_4 + 2CO_2(g) + 2H_2O(g) \quad (10)$$

$$6NiO + C_2H_4(g) \rightarrow 6Ni + 2CO_2(g) + 2H_2O(g) \quad (11)$$

$$6CoO + C_2H_4(g) \rightarrow 6Co + 2CO_2(g) + 2H_2O(g) \quad (12)$$

$$6Mn_3O_4 + C_2H_4(g) \rightarrow 18MnO + 2CO_2(g) + 2H_2O(g) \quad (13)$$

Thermal reduction involving H_2:

$$2LiCoO_2 + H_2(g) \rightarrow 2CoO + Li_2O + H_2O(g) \quad (14)$$

$$2LiNi_{0.6}Co_{0.2}Mn_{0.2}O_2 + H_2(g) \rightarrow 2/5CoO + 6/5NiO + MnO + Li_2O + H_2O(g) \quad (15)$$

$$2/3LiMn_2O_4 + H_2(g) \rightarrow 1/3Li_2O + 4/3Mn_3O_4 + H_2O(g) \quad (16)$$

$$NiO + H_2(g) \rightarrow Ni + 2H_2O(g) \quad (17)$$

$$CoO + H_2(g) \rightarrow Co + H_2O(g) \quad (18)$$

$$Mn_3O_4 + H_2(g) \rightarrow 3MnO + H_2O(g) \quad (19)$$

DFT calculations

All DFT calculations were conducted using the Vienna Ab-initio Simulation Package (VASP)[43,44]. The Perdew–Burke–Ernzerhof (PBE) functional within the generalized gradient approximation (GGA) method was used to account for the exchange-correlation effects[45,46]. Core–valence interactions were considered using the projected augmented wave (PAW) method[47]. The plane wave cutoff energy for the basis was set to 400 eV, and a 2 × 2 × 1 Monkhorst-Pack grid k-points were selected to sample the Brillouin zone integration. Structural optimization was carried out with energy convergence criteria set at 1.0×10^{-5} eV and force convergence criteria set at 0.02 eV $Å^{-1}$. Grimme's DFT-D3 methodology was used to describe the dispersion interactions[48].

The Gibbs free energy changes (ΔG) of the reaction are calculated using the following formula:

$$\Delta G = \Delta E + \Delta ZPE - T\Delta S + \Delta G_U + \Delta G_{pH} \quad (20)$$

where ΔE is the electronic energy difference directly obtained from DFT calculations, ΔZPE is the zero-point energy difference, T is the room temperature (298.15 K), and ΔS is the entropy change. ΔG_U is $-eU$, where U is the applied electrode potential. $\Delta G_{pH} = k_B T \times \ln 10 \times pH$, where k_B is the Boltzmann constant, and the pH value is set to 0.

Economic and environmental analysis

The EverBatt model was used to perform techno-economic and life cycle analysis of three waste battery recycling processes: pyrometallurgical (Pyro), hydrometallurgical (Hydro), and co-pyrolysis (Co-Pyro)[42]. The EverBatt Model 2023, developed by Argonne National Laboratory, can divide the Li battery closed-loop recycling process into two parts. The first part is the cost of machinery such as crushing and recycling costs, and the second part considers the cost of utilizing recycled raw materials and incorporating Li sources to achieve regeneration.

Data availability

All the data supporting the findings of this study are available within the article, source data, and supplementary information files. Source data, and supplementary information files. Source data are provided as a Source Data file. Source data are provided with this paper.

References

1. Chen, M. et al. Recycling end-of-life electric vehicle lithium-ion batteries. *Joule* **3**, 2622–2646 (2019).
2. Harper, G. et al. Recycling lithium-ion batteries from electric vehicles. *Nature* **575**, 75–86 (2019).
3. Fan, M. et al. Increased residual lithium compounds guided design for green recycling of spent lithium-ion cathodes. *Energy Environ. Sci.* **14**, 1461–1468 (2021).
4. Jehanno, C. et al. Critical advances and future opportunities in upcycling commodity polymers. *Nature* **603**, 803–814 (2022).
5. Wang, J. et al. Sustainable upcycling of spent $LiCoO_2$ to an ultra-stable battery cathode at high voltage. *Nat. Sustain.* **6**, 797–805 (2023).
6. Bauer, C. et al. Charging sustainable batteries. *Nat. Sustain.* **5**, 176–178 (2022).
7. Ellis, L. D. et al. Chemical and biological catalysis for plastics recycling and upcycling. *Nat. Catal.* **4**, 539–556 (2021).
8. Larcher, D. & Tarascon, J. M. Towards greener and more sustainable batteries for electrical energy storage. *Nat. Chem.* **7**, 19–29 (2015).
9. Qiu, X. et al. Enabling the sustainable recycling of $LiFePO_4$ from spent lithium-ion batteries. *Green. Chem.* **24**, 2506–2515 (2022).
10. Meng, Z. et al. Green and energy-saving recycling of $LiCoO_2$ by synergetic pyrolysis with polyvinyl chloride plastics. *ACS Sustain. Chem. Eng.* **10**, 12329–12341 (2022).
11. Huang, Z. et al. Hydrogen reduction of spent lithium-ion battery cathode material for metal recovery: mechanism and kinetics. *Front. Chem.* **10**, 1019493 (2022).
12. Tang, Y. et al. Recovery and regeneration of $LiCoO_2$-based spent lithium-ion batteries by a carbothermic reduction vacuum pyrolysis approach: controlling the recovery of CoO or Co. *Waste Manag.* **97**, 140–148 (2019).
13. Chen, X. et al. Selective recycling of valuable metals from waste $LiCoO_2$ cathode material of spent lithium-ion batteries through low-temperature thermochemistry. *Chem. Eng. J.* **434**, 134542 (2022).
14. Qu, X. et al. A vapor thermal approach to selective recycling of spent lithium-ion batteries. *Green. Chem.* **23**, 8673–8684 (2021).
15. Chen, X. et al. Microthermal catalytic aerogenesis of renewable biomass waste using cathode materials from spent lithium-ion batteries towards reversed regulated conversion and recycling of valuable metals. *Green. Chem.* **25**, 1559–1570 (2023).
16. Elkhalifa, S., Al-Ansari, T., Mackey, H. R. & McKay, G. Food waste to biochars through pyrolysis: a review. *Resour. Conserv. Recycl.* **144**, 310–320 (2019).
17. Qiu, B. et al. Recycling spent lithium-ion batteries using waste benzene-containing plastics: synergetic thermal reduction and benzene decomposition. *Environ. Sci. Technol.* **57**, 7599–7611 (2023).
18. Wang, M. M., Zhang, C. C. & Zhang, F. S. Recycling of spent lithium-ion battery with polyvinyl chloride by mechanochemical process. *Waste Manag.* **67**, 232–239 (2017).
19. Zhong, X. et al. Innovative methodology for green recycling of spent lithium-ion batteries: effective pyrolysis with DMF. *J. Clean. Prod.* **377**, 134503 (2022).
20. Mitrano, D. M., Wick, P. & Nowack, B. Placing nanoplastics in the context of global plastic pollution. *Nat. Nanotechnol.* **16**, 491–500 (2021).
21. Rosenboom, J.-G., Langer, R. & Traverso, G. Bioplastics for a circular economy. *Nat. Rev. Mater.* **7**, 117–137 (2022).
22. Lee, K., Jing, Y., Wang, Y. & Yan, N. A unified view on catalytic conversion of biomass and waste plastics. *Nat. Rev. Chem.* **6**, 635–652 (2022).
23. Jie, X. et al. Microwave-initiated catalytic deconstruction of plastic waste into hydrogen and high-value carbons. *Nat. Catal.* **3**, 902–912 (2020).
24. Zhang, H., Zhu, G., Yan, H., Li, T. & Zhao, Y. The mechanism on biomass reduction of low-grade manganese dioxide ore. *Met. Mater. Trans. B* **44**, 889–896 (2013).
25. Lombardo, G., Ebin, B., Foreman, M. R. J. St, Steenari, B.-M. & Petranikova, M. Chemical transformations in Li-ion battery electrode materials by carbothermic reduction. *ACS Sustain. Chem. Eng.* **7**, 13668–13679 (2019).
26. Wang, B., Wang, Y., Du, S., Zhu, J. & Ma, S. Upcycling of thermosetting polymers into high-value materials. *Mater. Horiz.* **10**, 41–51 (2023).
27. Zhu, Y., Romain, C. & Williams, C. K. Sustainable polymers from renewable resources. *Nature* **540**, 354–362 (2016).
28. Xu, Z. et al. Cascade degradation and upcycling of polystyrene waste to high-value chemicals. *Proc. Natl Acad. Sci. USA* **119**, e2203346119 (2022).
29. Dai, L. et al. Pyrolysis technology for plastic waste recycling: a state-of-the-art review. *Prog. Energy Combust. Sci.* **93**, 101021 (2022).
30. Chu, S. et al. Photocatalytic conversion of plastic waste: from photodegradation to photosynthesis. *Adv. Energy Mater.* **12**, 2200435 (2022).
31. Dong, F., Han, W., Han, W. & Tang, Z. Assembling core-shell SiO_2@NiaCobOx nanotube decorated by hierarchical NiCo-Phyllisilicate ultrathin nanosheets for highly efficient catalytic combustion of VOCs. *Appl. Catal. B.* **315**, 121524 (2022).
32. Jiang, Y. et al. Scalable decomposition-catalysis of disposable COVID-19 face mask over self-assembly metal-doping carbocatalysts for tunable value-added products. *Appl. Catal. B.* **317**, 121735 (2022).
33. Tian, W.-W., Ren, J.-T. & Yuan, Z.-Y. In-situ cobalt-nickel alloy catalyzed nitrogen-doped carbon nanotube arrays as superior free-standing air electrodes for flexible zinc-air and aluminum-air batteries. *Appl. Catal. B.* **317**, 121764 (2022).
34. Wen, X. et al. Nanosized carbon black combined with Ni_2O_3 as "universal" catalysts for synergistically catalyzing carbonization of polyolefin wastes to synthesize carbon nanotubes and application for supercapacitors. *Environ. Sci. Technol.* **48**, 4048–4055 (2014).
35. Li, M. et al. Synthesis strategies of carbon nanotube supported and confined catalysts for thermal catalysis. *Chem. Eng. J.* **431**, 133970 (2022).
36. Hou, P.-X., Liu, C. & Cheng, H.-M. Purification of carbon nanotubes. *Carbon* **46**, 2003–2025 (2008).
37. Kiciński, W. & Dyjak, S. Transition metal impurities in carbon-based materials: pitfalls, artifacts and deleterious effects. *Carbon* **168**, 748–845 (2020).
38. Mond, L., Langer, C. & Quincke, F. Action of carbon monoxide on nickel. *J. Chem. Soc. Trans.* **57**, 749–753 (1890).
39. Jung, E. et al. Atomic-level tuning of Co–N–C catalyst for high-performance electrochemical H_2O_2 production. *Nat. Mater.* **19**, 436–442 (2020).
40. Li, B. Q., Zhao, C. X., Liu, J. N. & Zhang, Q. Electrosynthesis of hydrogen peroxide synergistically catalyzed by atomic Co–Nx–C sites and oxygen functional groups in noble-metal-free electrocatalysts. *Adv. Mater.* **31**, e1808173 (2019).
41. Lu, Z. et al. High-efficiency oxygen reduction to hydrogen peroxide catalysed by oxidized carbon materials. *Nat. Catal.* **1**, 156–162 (2018).
42. Dai, Q. et al. EverBatt: a closed-loop battery recycling cost and environmental impacts model. Argonne National Laboratory,

United States. https://www.anl.gov/argonne-scientific-publications/pub/153050. (2019).
43. Kresse, G. & Hafner, J. Ab initio molecular dynamics for liquid metals. *Phys. Rev. B Condens. Matter* **47**, 558–561 (1993).
44. Kresse, G. & Hafner, J. Ab initio molecular-dynamics simulation of the liquid-metal-amorphous-semiconductor transition in germanium. *Phys. Rev. B Condens. Matter* **49**, 14251–14269 (1994).
45. Perdew, J. P., Burke, K. & Ernzerhof, M. Generalized gradient approximation made simple. *Phys. Rev. Lett.* **77**, 3865–3868 (1996).
46. Kresse, G. & From, D. J. Ultrasoft pseudopotentials to the projector augmented-wave method. *Phys. Rev. B* **59**, 1758–1775 (1999).
47. Blochl, P. E. Projector augmented-wave method. *Phys. Rev. B Condens. Matter* **50**, 17953–17979 (1994).
48. Grimme, S., Antony, J., Ehrlich, S. & Krieg, H. A consistent and accurate ab initio parametrization of density functional dispersion correction (DFT-D) for the 94 elements H-Pu. *J. Chem. Phys.* **132**, 154104 (2010).

Acknowledgements

We greatly thank the financial support from the Fundamental Research Funds for the Central Universities (2042023kf0214, H.Y.Y.), the National Natural Science Foundation of China (51874082, 52374308, H.Y.Y.), NSFC-Liaoning Joint Fund (U1908224, H.Y.Y.), Environmental Protection Department of the Hong Kong Government (GTF202020051, L.Y.S.L.), and Shenzhen Science, Technology and Innovation Commission (JCYJ20220818102210023, L.Y.S.L.).

Author contributions

H.Y. and L.Y.S.L. conceived and supervised the project. B.Q. performed the sample synthesis, characterization, and measurements. M.L. carried out the TEM, and XPS measurement and provide analysis. X.Q. collected the HSC data. Z.Y. provided the Everbatt Model. B.Q. and M.L. wrote the manuscript, and H.Y., L.Y.S.L., H.X., and D.W. revised it. All the authors contributed to the whole manuscript.

Competing interests

The authors declare no competing interests.

Additional information

Supplementary information The online version contains supplementary material available at https://doi.org/10.1038/s41467-024-50679-1.

Correspondence and requests for materials should be addressed to Lawrence Yoon Suk Lee or Huayi Yin.

Peer review information *Nature Communications* thanks Minseong Ko, Renjie Chen, and the other, anonymous, reviewer(s) for their contribution to the peer review of this work. A peer review file is available.